PNAS
www.pnas.org

Supplementary Information for

Ambidextrous Helical Nanotubes from Self-Assembly of Designed Helical Hairpin Motifs

Spencer A. Hughes[1], Fengbin Wang[2], Shengyuan Wang[1], Mark A.B. Kreutzberger[2], Tomasz Osinski[2], Albina Orlova[2], Joseph S. Wall[3], Xiaobing Zuo[4], Edward H. Egelman[2], and Vincent P. Conticello[1]*

Vincent P. Conticello
Email: vcontic@emory.edu

This PDF file includes:

Supplementary text
Figs. S1 to S30
References for SI reference citations

www.pnas.org/cgi/doi/10.1073/pnas.1903910116

Supplementary Information Text

Chemicals and Materials. All chemical reagents were purchased from Sigma-Aldrich Chemical Co. (St. Louis, MO) or Anaspec, Inc. (Fremont, CA) unless otherwise specified. The **HEAT_R1**, **HEAT_dimer**, and **LRV_dimer** peptides were ordered from GenScript USA, Inc. (Piscataway, NJ). Peptide synthesis resin was ordered from Applied Biosystems (Foster City, CA).

Experimental Methods

Peptide Synthesis. The **LRV_M3Δ1**, **HEAT_R1_W17F,** and **HEAT_R1_AW** peptides were prepared via microwave-assisted solid phase peptide synthesis on a CEM Liberty instrument as the *N*-acetyl, *C*-amide capped derivatives. A PAL-PEG-PS resin from Applied Biosystems was used for both peptides. Standard Fmoc protection chemistry was utilized in conjunction with coupling cycles consisting of HBTU/DIEA-mediated activation protocols and base-induced deprotection (20% piperidine in *N, N*-dimethylformamide with 0.1 M hydroxybenzotriazole) of the Fmoc group. The peptides were cleaved from the resin by incubation at room temperature for 3 hours in a cocktail consisting of trifluoroacetic acid (TFA), distilled water, triisopropylsilane, and 2,2'-(ethylenedioxy)-diethanethiol. Cleavage was followed by filtration and subsequent precipitation in diethyl ether. The peptide/diethyl ether mixture was then centrifuged at 4 °C at 4,000 rpm for 10 min. The supernatant was then discarded, and the precipitate allowed to desiccate overnight. Following desiccation, the crude peptide gels were resolubilized in 3 mL of a 50:50 mixture of acetonitrile and water (0.1% TFA additive) and purified by reversed-phase high-pressure liquid chromatography (HPLC) on a C18 column with a water-acetonitrile (0.1% TFA-additive) gradient. Peptide mass was confirmed using MALDI mass spectrometry. Purified HPLC fractions were then lyophilized, sealed, and stored at -30 °C.

Peptide Assembly. Stock solutions of **HEAT_R1, HEAT_R1_W17F, HEAT_R1_AW,** and **HEAT_dimer** (3 mg·mL^{-1}) were prepared by solubilizing 0.6 mg of purified, lyophilized peptide in 200 μL of 10 mM MES buffer, pH 6.0. Immediately after mixture, the solution was titrated to pH 6.0 using dilute sodium hydroxide solution. Stock solutions of **LRV_M3Δ1** and **LRV_dimer** (3 mg·mL^{-1}) were prepared by solubilizing 0.6 mg of purified, lyophilized peptide in 200 μL of 10 mM MES buffer, pH 6.0. Immediately after mixture, the solution was titrated to pH 6.0 using dilute sodium hydroxide solution. This solution was then thermally annealed using the following thermal cycler protocol: (1) rapid heating to 90° C for 30 minutes and (2) cooling to 25°C at a rate of -0.2°C/minute.

Circular Dichroism Spectropolarimetry. CD measurements were performed on a Jasco J-810 CD spectropolarimeter using 0.10 mm thick quartz plates (Hellma Analytics). Spectra were collected at 50 nm/min. in the range of 190-260 nm, and a data pitch of 0.2 nm. CD melts were performed on the same instrument, with the same cuvette, monitoring the 222 nm peak from 20º C to 90º C, with a +1ºC/min. gradient.

Transmission Electron Microscopy. TEM grids were prepared using solutions of peptide (3 mg·mL^{-1}) in aqueous buffer (10 mM acetate, pH 5.0, and 10 mM MES, pH 6.0, 10 mM MOPS, pH 7.0, and 10 mM TAPS, pH 8.0). Samples were prepared by depositing 4 μL of peptide solution onto a 200-mesh carbon-coated copper grid from Electron Microscopy Services (Hatfield, PA). After 1.5 minutes of incubation on the grid, moisture was wicked away, leaving only a thin film of

sample. 4 μL of negative stain (2% methylamine tungstate) was deposited onto the thin film, to allow proper mixture. After 1 minute of staining, the remaining moisture was wicked away, and the grid dried overnight in a tabletop desiccator. Electron micrographs were captured on a Hitachi HT-7700 with a tungsten filament and AMT CCD camera, at an accelerating voltage of 80 kV.

Cryo-electron microscopy and image processing. The **HEAT_R1** peptide (4 μL of a 3 mg·mL^{-1} solution) was applied to glow-discharged lacey carbon grids and vitrified in a Vitrobot Mark IV (FEI, Inc.). Grids were imaged in a Titan Krios at 300 keV and recorded with a Falcon II direct electron detector at 1.05 Å per pixel. Images were collected using a defocus range of 0.5–3.0 μm, with a total exposure of 2 s (amounting to 70 electrons·Å^{-2}) dose-fractionated into seven chunks. All the images were first motion corrected by the MotionCorr v2 (1), and then the CTFFIND3 (2) program was used for determining the actual defocus of the images. Images with poor CTF estimation as well as defocus > 3 μm were discarded. A total of 386 images were selected and peptide filaments of varying lengths were boxed using the e2helixboxer program within EMAN2 (3). The CTF was corrected by multiplying the images from the first two chunks (containing a dose of ~ 20 electrons·Å^{-2}) with the theoretical CTF.

Overlapping 256-px long boxes with a shift of 5 pixels (~ 1.5 times of the axial rise) were cut from the long filaments. The determination of the helical symmetry was by trial and error, searching for a symmetry which yielded recognizable secondary structure. Power spectra from the filaments suggested a variability in the helical parameters. A reference-based sorting procedure was used to bin the segments based on the axial rise and azimuthal rotation. Then 56,421 out of 356,100 segments were selected after this sorting and the IHRSR (4) method implemented in in Spider (5) was used to produce the final reconstructions at ~6 Å. The helical hand was determined by the fit of crystal structures into the cryo-EM map.

The **LRV_M3Δ1** peptide (4 μL of a ~3 mg·mL^{-1} solution) was plunge-frozen in the same manner as the **HEAT_R1** filament. The **LRV_M3Δ1** grids were imaged using the Titan Krios at the National Cancer Institute and recorded with a K2 camera at 1.32 Å per pixel without super-resolution. A total of 296 images were selected, motion-corrected and CTF-corrected in a similar way with the **HEAT_R1** peptide. Then 512-px long overlapping boxes with a shift of 8 pixels, containing a dose of circa 20 electrons·Å^{-2}, were cut out from the CTF-corrected images and were used in the initial IHRSR reconstruction. The helical symmetry was also determined by trial and error, searching for a symmetry which yielded recognizable secondary structure. After determining the correct symmetry, segments were sorted using a reference-based procedure based on the azimuthal rotation. Then 62,616 out of 171,324 segments were selected and were further reconstructed by the IHRSR method in Spider. After the last cycle of the reconstruction, the alignment parameters were applied to an image stack containing 10 electrons·Å^{-2}. The final volume generated from the lower dose image stack had a resolution of ~ 4.4 Å. The correct helical hand could be directly determined from the hand of the α-helices visible at this resolution.

Model building. The initial model of the **HEAT_R1** peptide was generated by Phyre2 (6) homology modeling using residues 74-103 of 4JW3 (7), a concatemeric polypeptide derived from consensus PBS_HEAT repeats similar to 3LTJ, as the starting model (80% sequence identity). Then the map corresponding to a **HEAT_R1** dimer was segmented from the experimental filament map in Chimera (8). At this resolution, the N/C- termini of the peptide subunits in the dimer cannot be distinguished directly from the density. There are 4 possible arrangements of the peptide dimer termini viewing from outside of the filament and from left to right: (1) N-N; (2) C-C; (3) N-C; (4) C-N. All those four possibilities were examined by docking peptide subunits into the segmented map followed by a Phenix real-space refinement. The N-N arrangement fit the map significantly better, with at least 20% higher real-space coefficient correlation than the other possibilities. A filament model was generated and further refined using Phenix (9), and MolProbity (10) was used to evaluate the quality of the filament model. The refinement statistics are given in Table 1.

The initial model of the **LRV_M3Δ1** peptide was generated by extracting the backbone from 1LRV using residues 124-146 as the starting model. The map corresponding to the model positioned in the filament was segmented from the experimental map at 6 Å radius in Chimera. The **LRV_M3Δ1** model was rebuilt with the RosettaCM (11) protocol. To obtain a well-fitting model a total of 1000 decoy models were generated based on the segmented map. Rosetta's energy function was used to select the top 5 models from which the best fitting was chosen for further processing. Coot was used to manually edit the model to better reflect actual stereochemistry, and then it was further refined by Phenix real-space refinement protocol. Then the symmetry-related molecules were regenerated using Rosetta, and the whole assembly was further refined in Phenix real-space refinement. The quality of the filament model was assessed by MolProbity. The refinement statistics are given in Table 1. Cryo-EM maps and atomic coordinates have been deposited with the Electron Microscopy Data Bank and Protein Data Bank with accession codes given in Table 1.

Scanning Transmission Electron Microscopy. STEM data were acquired at Brookhaven National Laboratory (BNL). The STEM instrument operates at 40 keV with a scanning probe of < 0.3 nm diameter produced from a cold field-emission source. Each electron emerging from the specimen is detected by one of the scintillator photomultiplier detectors collecting 0−15 mRadian (bright field), 15−40 mRadian (small-angle dark field) and 40−200 mRadian (large-angle dark field). The large-angle signal is proportional to the mass of atoms in the path of the beam. Specimen quality and mass calibration were assessed by detailed comparison of the image to the known structure of tobacco mosaic virus (TMV). For mass-per-length (M/L) measurements, TMV rafts at a theoretical M/L value of 13.1 kDa/Å were employed for calibration.

HEAT_R1 was assembled at 3 mg·mL^{-1} in 10 mM MES buffer, pH 6.0. **LRV_M3Δ1** was assembled at 3 mg·mL^{-1} in 10 mM MES buffer, pH 6.0, then thermally annealed as previously described. These solutions were then diluted to 0.3 mg·mL^{-1} and 0.03 mg·mL^{-1} for the unstained STEM imaging, and to 0.1 mg·mL^{-1} for negative-stained STEM imaging. Specimens are deposited on thin carbon (circa 2 nm thick) supported on a thicker holey carbon film mounted on a titanium grid using the wet-film, hanging-drop method. TMV is added to the grid first as an internal control, followed by injection buffer, then specimen solution (in 10 mM MES buffer, pH 6.0) for 1 min, then 10 washes of 20 mM ammonium acetate pH 7.0. Excess solution is wicked from the edge with filter paper between each injection. After the last wash, the grid is wicked to a thin layer (ca. 1 mm), fast frozen by plunging into liquid nitrogen slush and stored under liquid nitrogen. Grids are freeze-dried overnight in an ion pumped chamber with an efficient cold trap and transferred under vacuum to the STEM cold stage (−160 °C). Imaging typically uses a dose of 20 $e^{-}/Å^2$ (causing < 5% mass loss, corrected by comparison to TMV). Mass measurements were performed off-line with the customized software PCMass32.

Small- and Wide-Angle X-Ray Scattering Measurements. Synchrotron SAXS/WAXS measurements were taken at the 12-ID-B beamline of the Advanced Photon Source at Argonne National Laboratory in Lemont, Illinois. **HEAT_R1, HEAT_R1_W17F,** and **HEAT_dimer** were assembled at 6 mg·mL^{-1} in 10 mM MES buffer, pH 6.0. **LRV_M3Δ1** and **LRV_dimer** were assembled at 6 mg·mL^{-1} in 10 mM MES buffer, pH 6.0, then thermally annealed as previously described. These solutions were then dialyzed into 10 MES buffer, pH 6.0 with a 1% glycerol additive to stabilize against X-ray radiation damage. SAXS/WAXS measurements were then taken on the peptide solutions at 25 °C in a quartz capillary flow cell (1.5 mm). The solutions were raised and lowered in the flow cell to minimize radiation damage. Twenty 2D images were collected per sample, and then azimuthally averaged into 1D SAXS scattering curves after solid angle correction and normalization against the transmitted X-ray beam intensity, using the software package at beamline 12-ID-B. The 1D scattering curves were then averaged, and the averaged signal from the MES buffer was subtracted out.

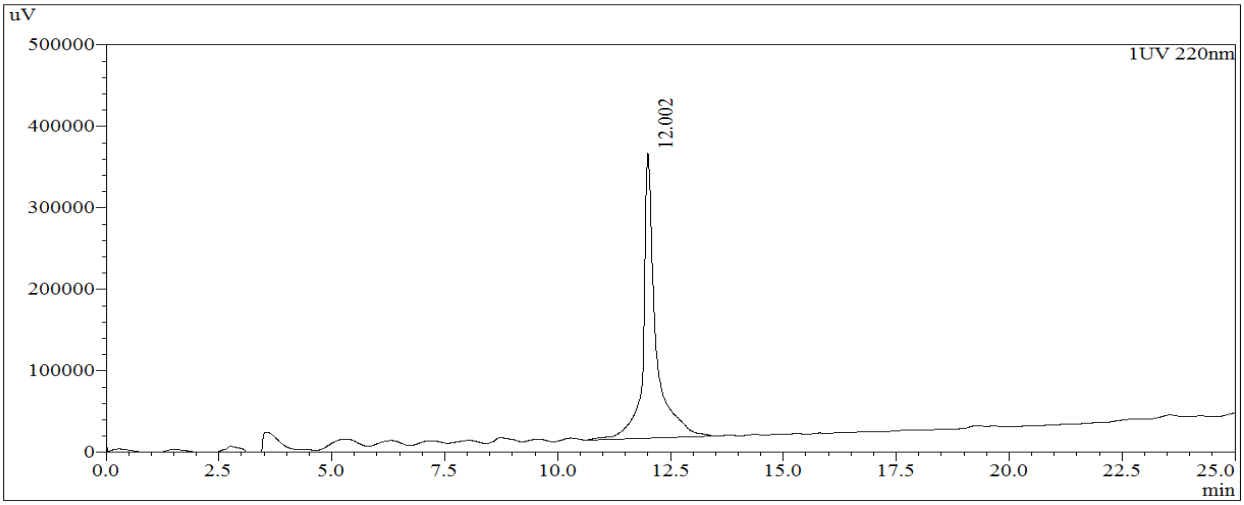

Fig. S1. Reverse-phase analytical HPLC trace of **HEAT_R1.**

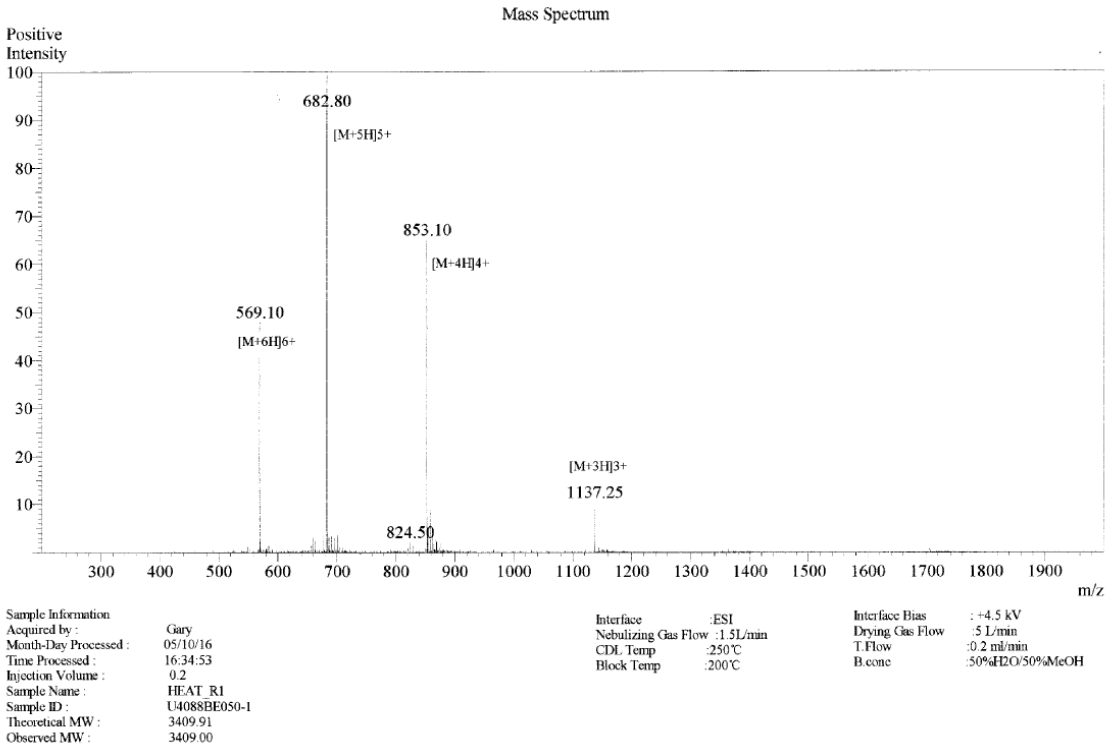

Fig. S2. Electrospray-ionization (ESI) mass spectrum of **HEAT_R1.**

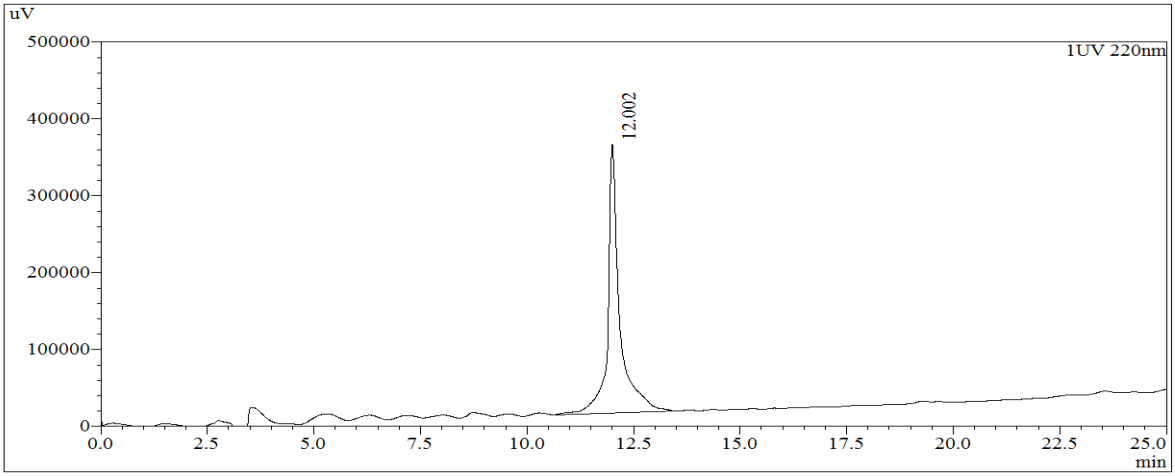

Fig. S3. Reverse-phase analytical HPLC trace of **LRV_M3Δ1.**

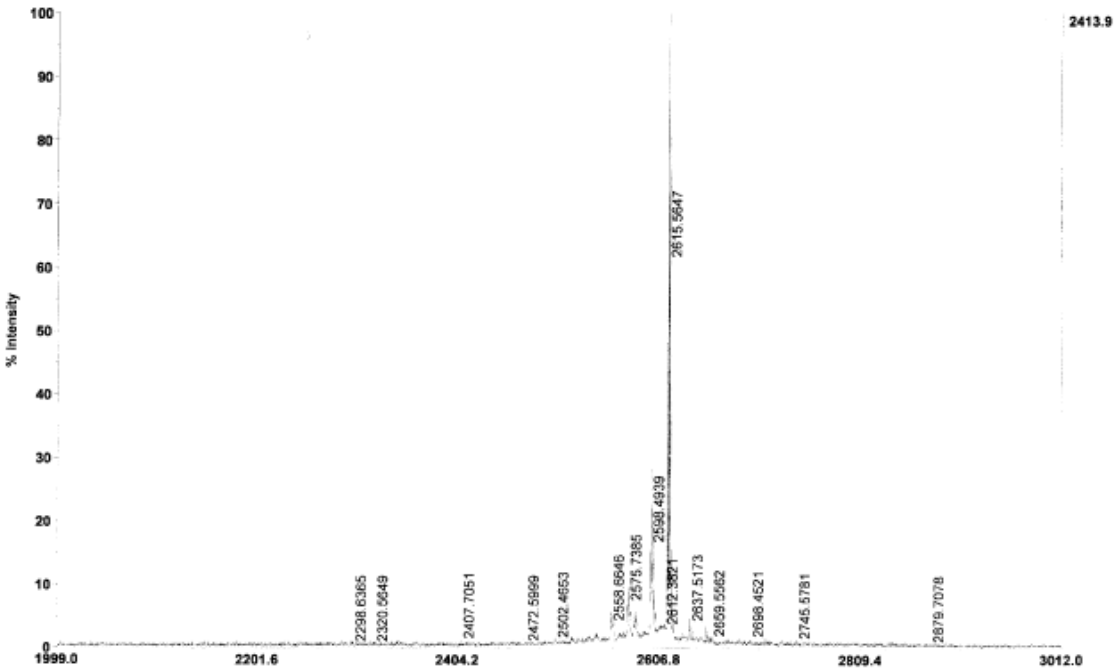

Fig. S4. MALDI-TOF mass spectrum of **LRV_M3Δ1.**

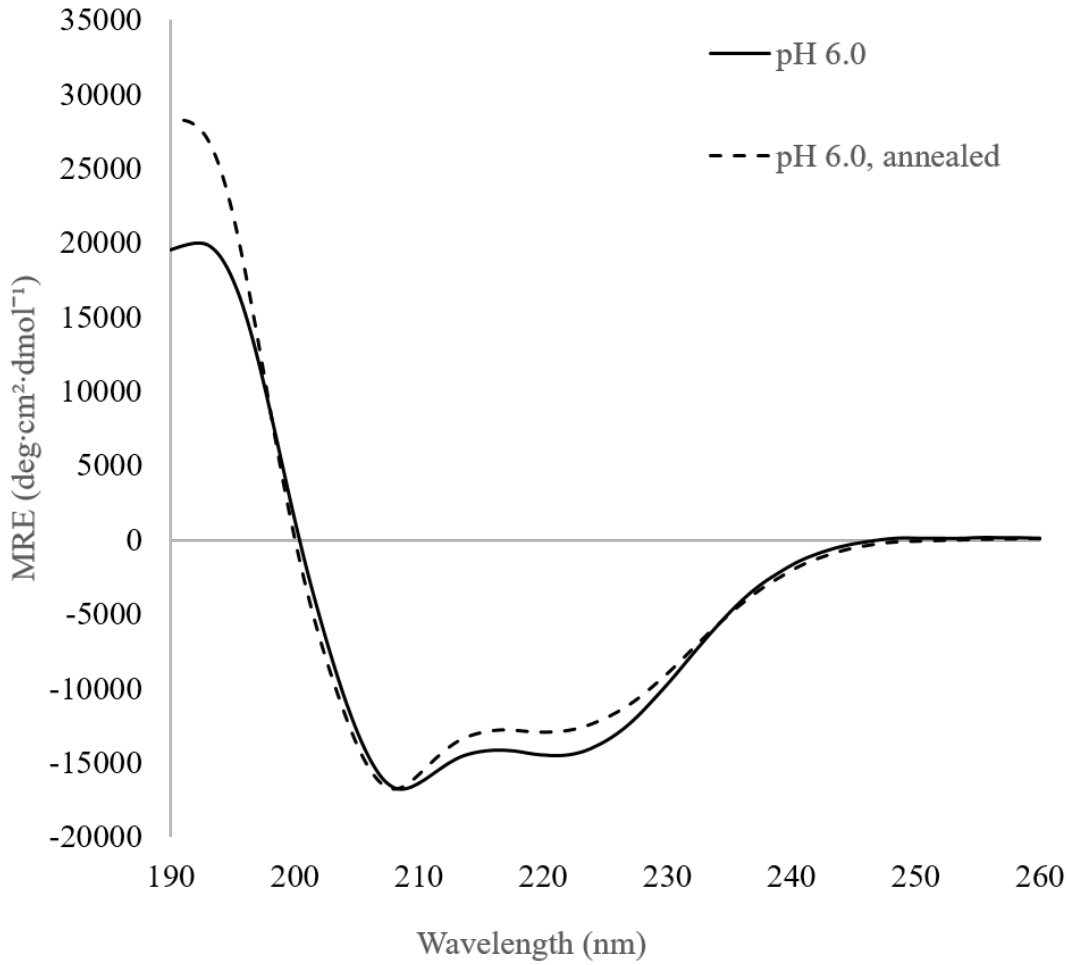

Fig. S5. Circular Dichroism (CD) spectra for **HEAT_R1** under optimal conditions (250 μM peptide concentration, 10 mM MES, pH 6.0).

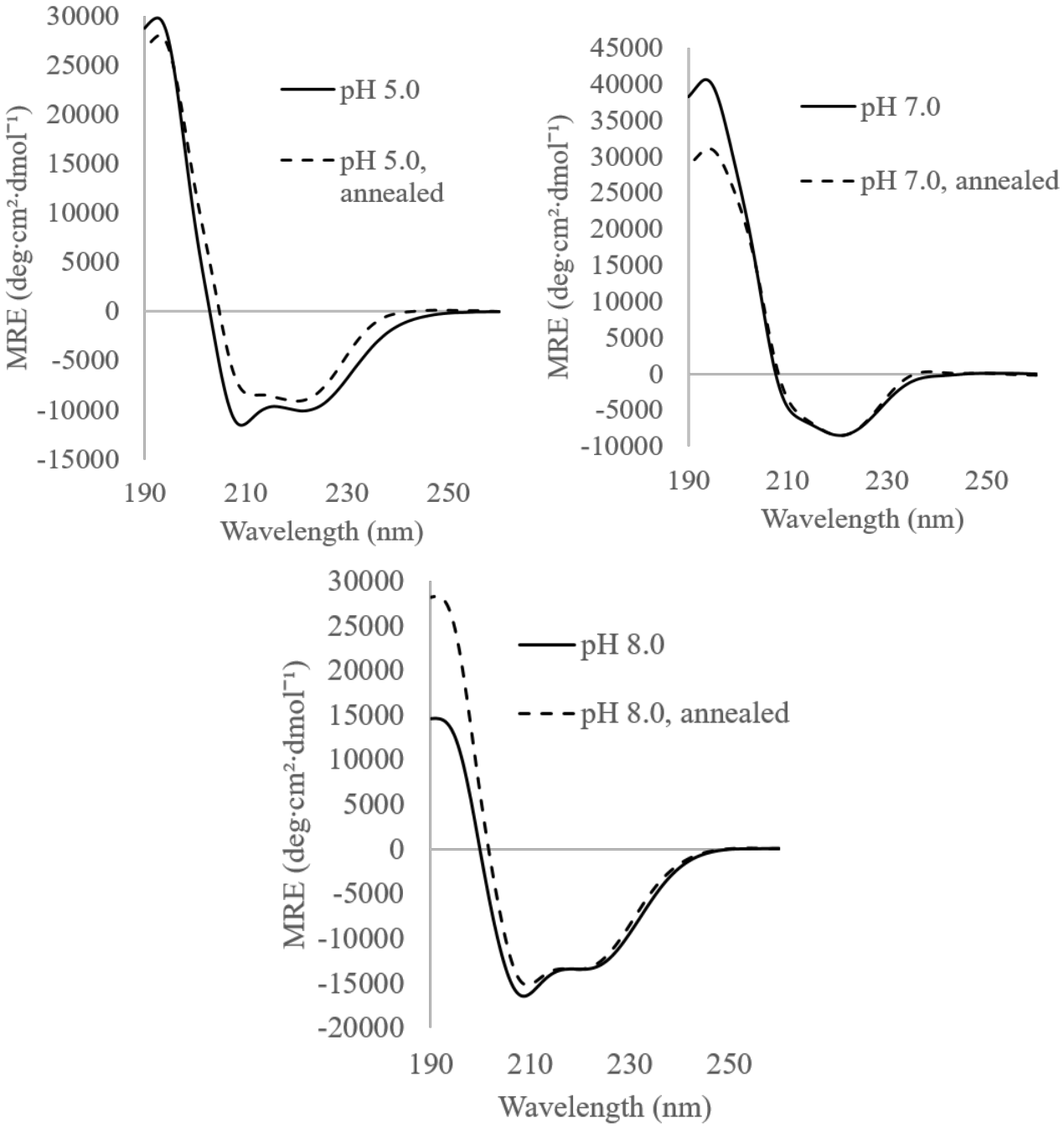

Fig. S6. CD spectra for **HEAT_R1** at pH 5.0, pH 7.0, and pH 8.0 (all taken at 250 μM peptide concentrations). Buffers were 10 mM Acetate (pH 5.0), 10 mM MOPS (pH 7.0), and 10 mM TAPS (pH 8.0).

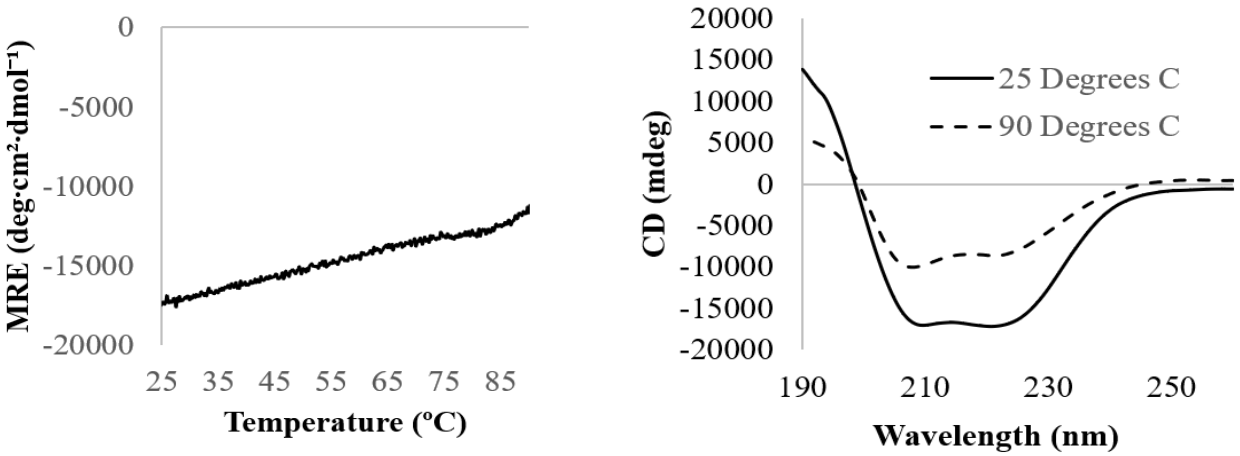

Fig. S7. Variable Temperature CD Scan of **HEAT_R1**. The CD signal at 222 nm was monitored from 25-90 °C (left), at a 250 μM peptide concentration. No thermal transition was observed; a standard CD spectrum was collected at 90º C (right). A helical CD signature was observed at both temperatures.

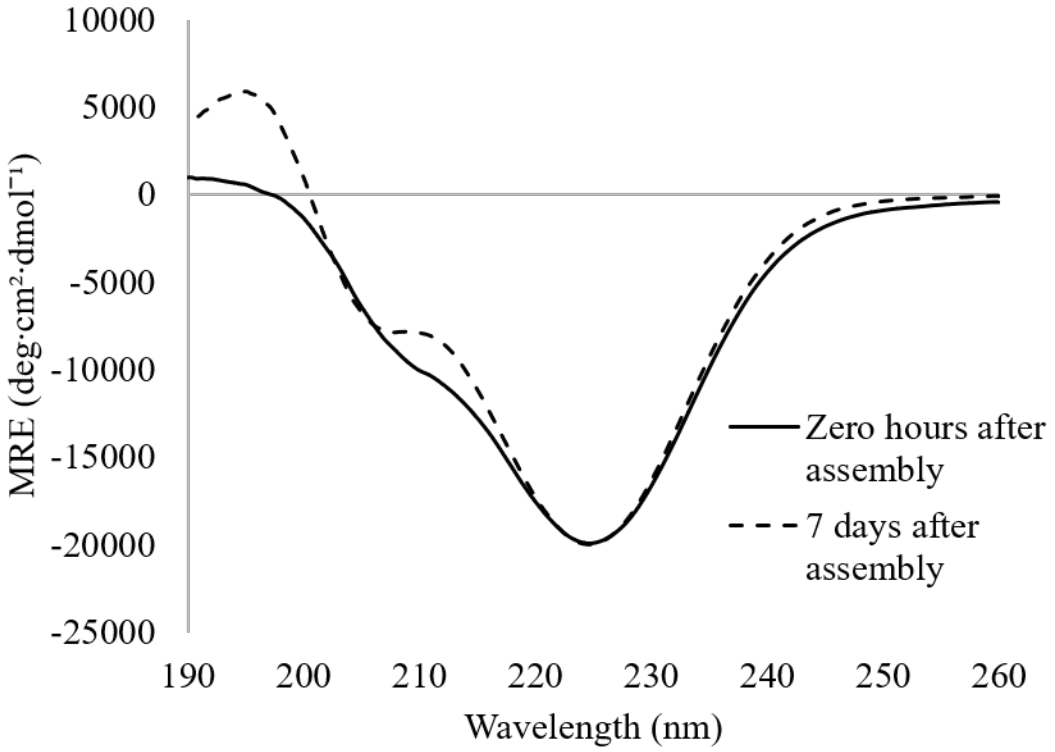

Fig. S8. Time-dependence of circular dichroism spectra for **LRV_M3Δ1** over time (450 μM peptide concentration, 10 mM MES, pH 6.0).

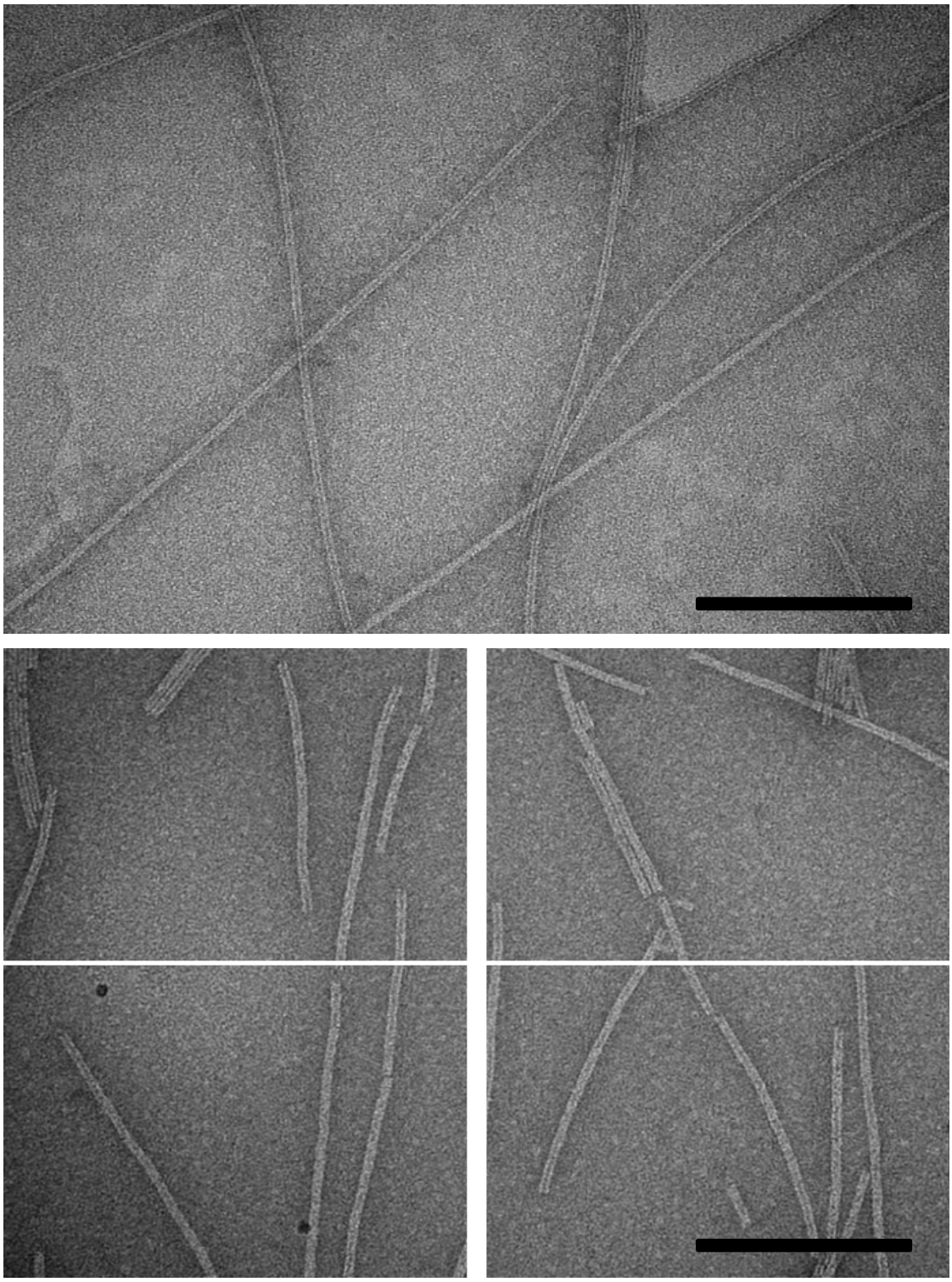

Fig. S9. Representative negatively stained TEM images of **LRV_M3Δ1** (top) and **HEAT_R1** (bottom) filaments**.** Scale bars are 100 nm.

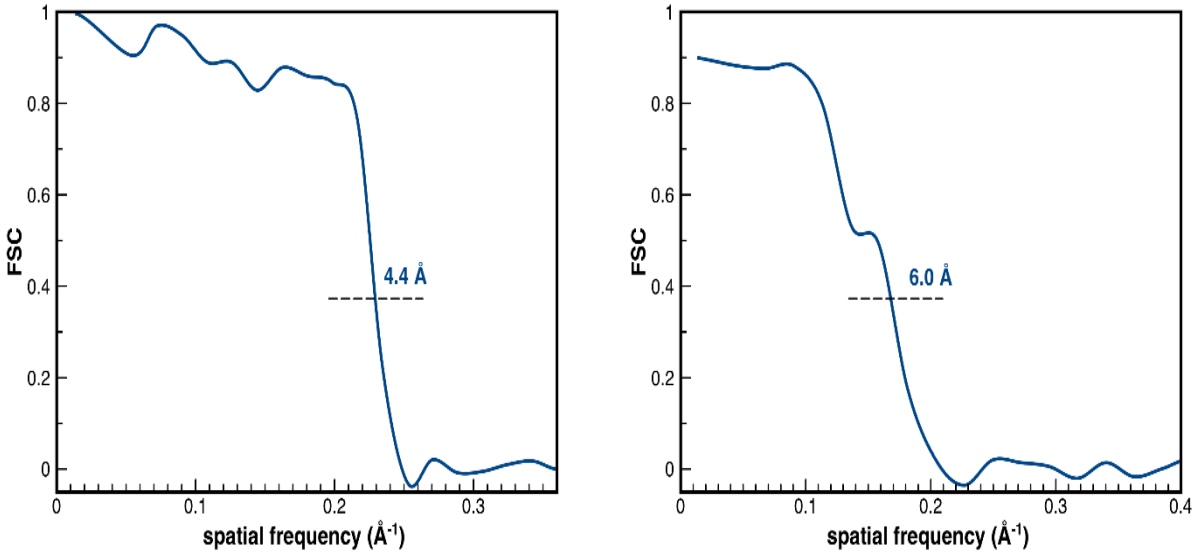

Fig. S10. Model:Map (12) Fourier Shell Correlation (FSC) plots for **LRV_M3Δ1** (left) and **HEAT_R1** (right) indicating the resolution of the two cryo-EM structures (4.4 Å and 6.0 Å) respectively. The cut-off was set at 0.38.

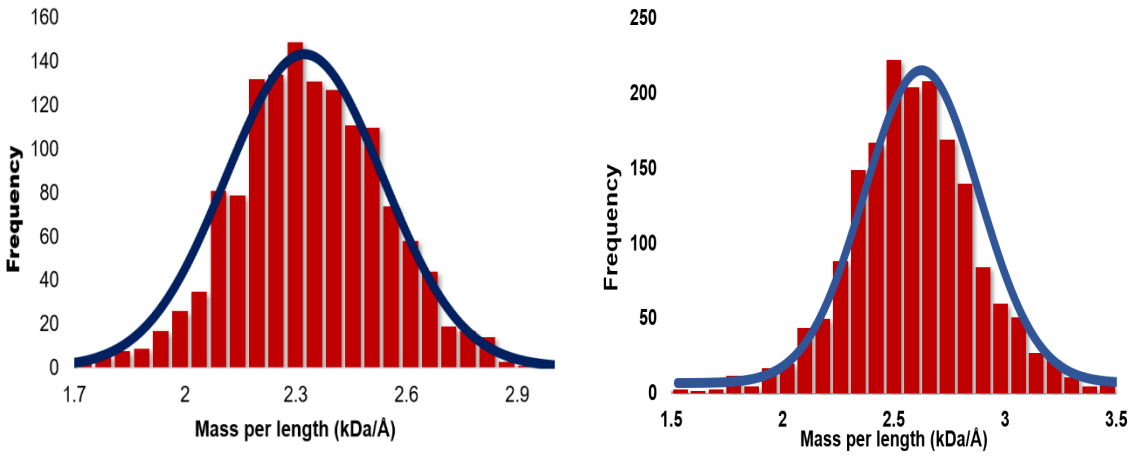

Fig. S11. STEM-derived mass per length (MPL) distribution for **HEAT_R1** (A) and **LRV_M3Δ1** (B) filaments. Overlaid in navy blue is a Gaussian curve for comparison. MPL values were calculated to be 2356 ± 214 Da·Å^{-1} and 2697 ± 258 Da·Å^{-1} for **HEAT_R1** and **LRV_M3Δ1** respectively.

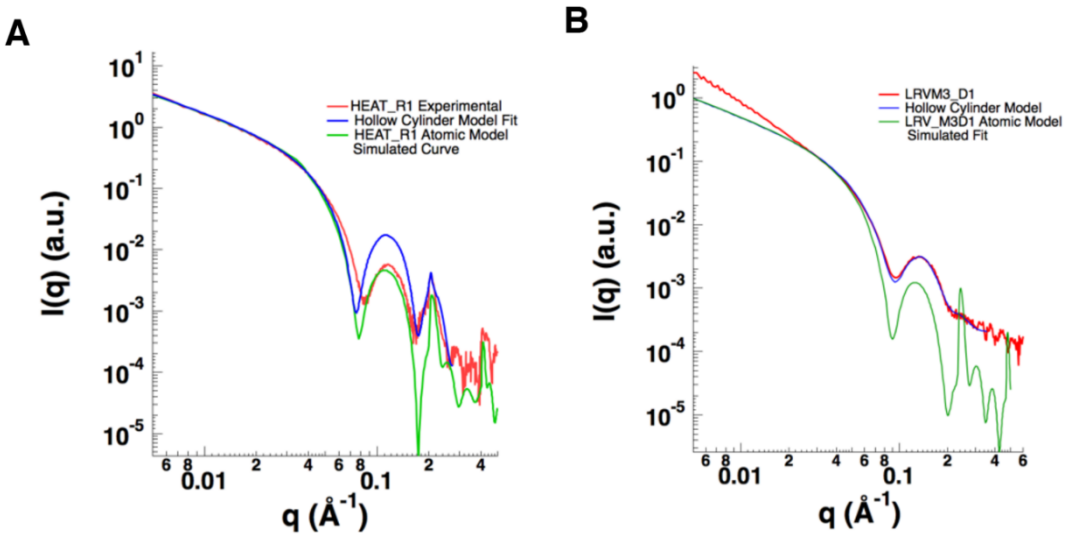

Fig. S12. Synchrotron SAXS scattering curves for buffered aqueous solutions of **HEAT_R1** (A) and **LRV_M3Δ1** (B) filaments. Red curve: experimental data, blue curve: fit with hollow cylinder model, green curve: calculated from the respective atomic structural models (length ~300nm). For **HEAT_R1**, the low q (< 0.02 Å^{-1}) intensities follow the q^{-1} power law, indicating the assembly adopts a long rod like shape. The well-defined oscillation feature in q of 0.05-0.30 Å^{-1}indicates a highly uniformed cross-section size. The diffraction peak at ~0.206 Å^{-1} arises from the ordered helical structure, with a pitch of ~ 30.5 Å. For **LRV_M3Δ1**, the experimental SAXS curve shows an oscillation feature, reflecting the cylindrical shape. The absence of a diffraction peak at ~0.24 Å^{-1}, as depicted in the simulated curve (green), indicates that the **LRV_M3Δ1** filaments lack long order in the helical structure. Both peptides were assembled at 6 mg·mL^{-1} and dialyzed against 10 mM MES buffer (pH 6.0) with 1% v/v glycerol. **LRV_M3Δ1** was thermally annealed (as previously described) prior to dialysis.

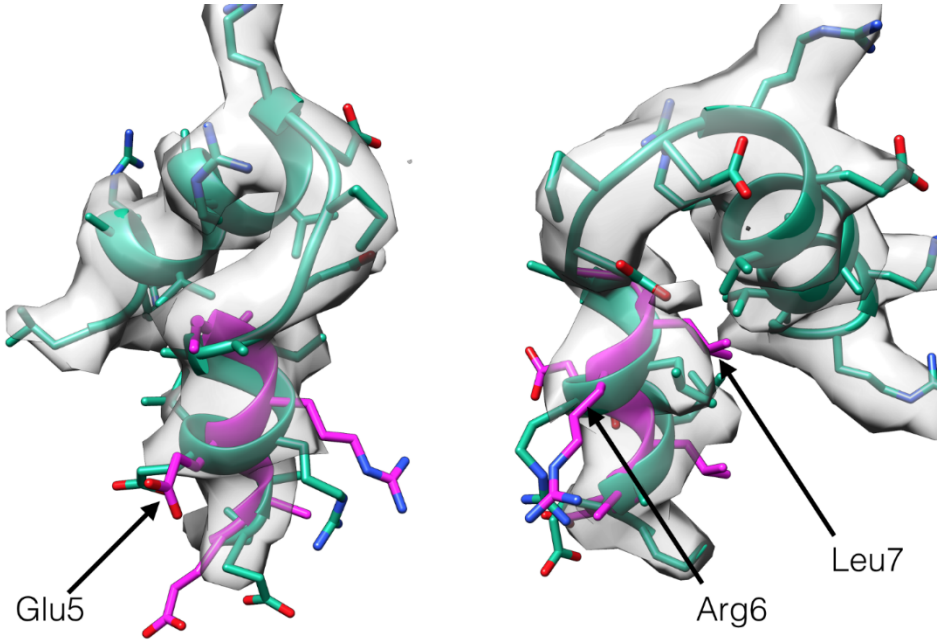

Fig. S13. Secondary structural analysis of **LRV_M3Δ1** based on the cryo-EM reconstruction. Represented in gray is the observed electron density in the cryo-EM map; fit into this density are the two candidate secondary structures. An α/α subunit is represented in green, and a single 3_{10} helix is represented in purple. Though the hypothetical subunit composition is α/3_{10}, the observed density is more consistent with an α/α subunit. Several clashing residues have been noted with black arrows.

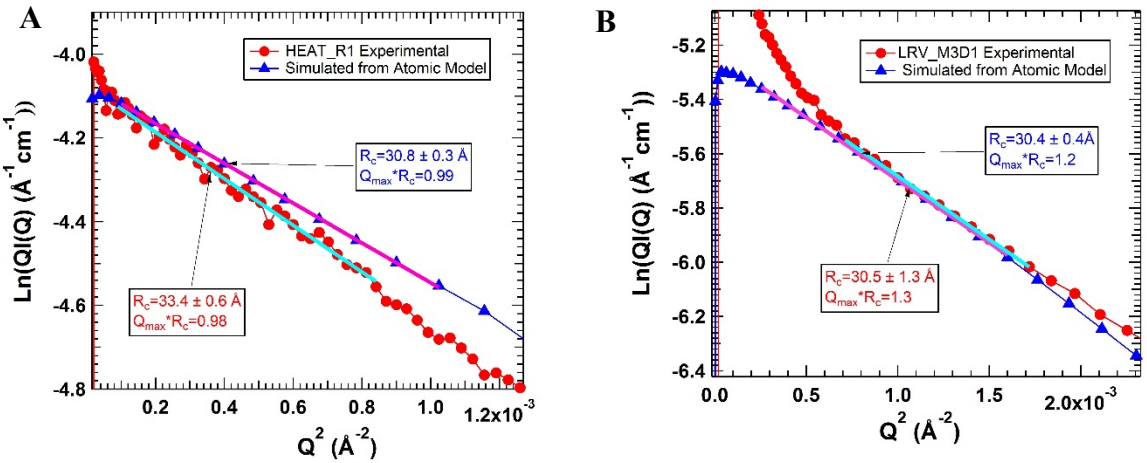

Fig. S14. Modified Guinier fit for rod-like forms of synchrotron SAXS scattering data for buffered aqueous solutions of **HEAT_R1** (A) and **LRV_M3Δ1** (B) filaments. Experimental data shown in red solid circle symbols; simulated data from atomic models in solid triangle symbols. Note that for **LRV_M3Δ1**, the experimental SAXS data at the low q region deviates from q^{-1} power law, possibly caused by presence of higher order aggregates.

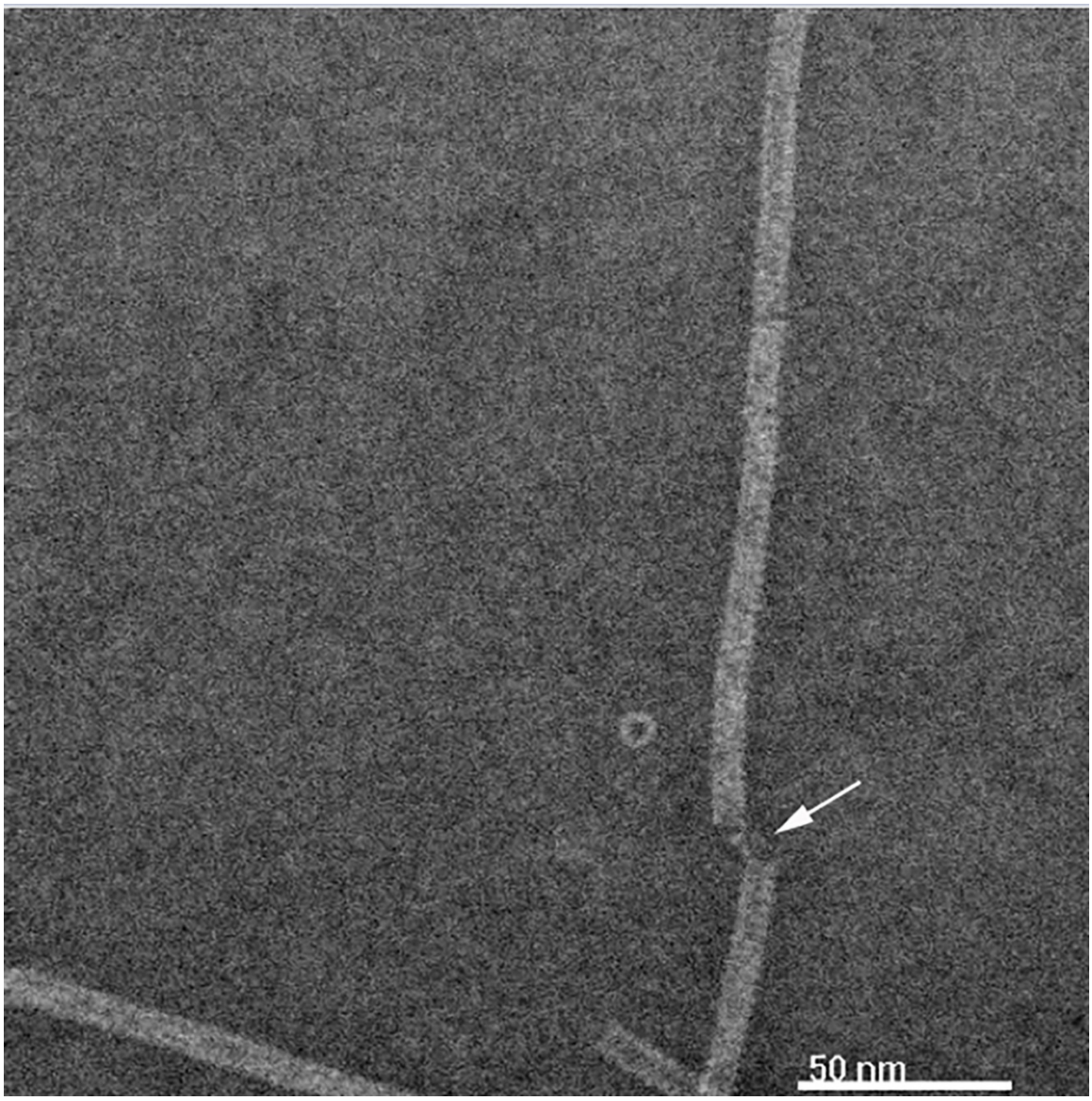

Fig. S15. Negatively-stained STEM image of **HEAT_R1** filaments, in which localized helical unwinding can be observed (white arrow). Note that the hollow cylindrical cross-section can be observed for a tubular fragment that has adventitiously adsorbed with the helical axis oriented perpendicular to the grid surface.

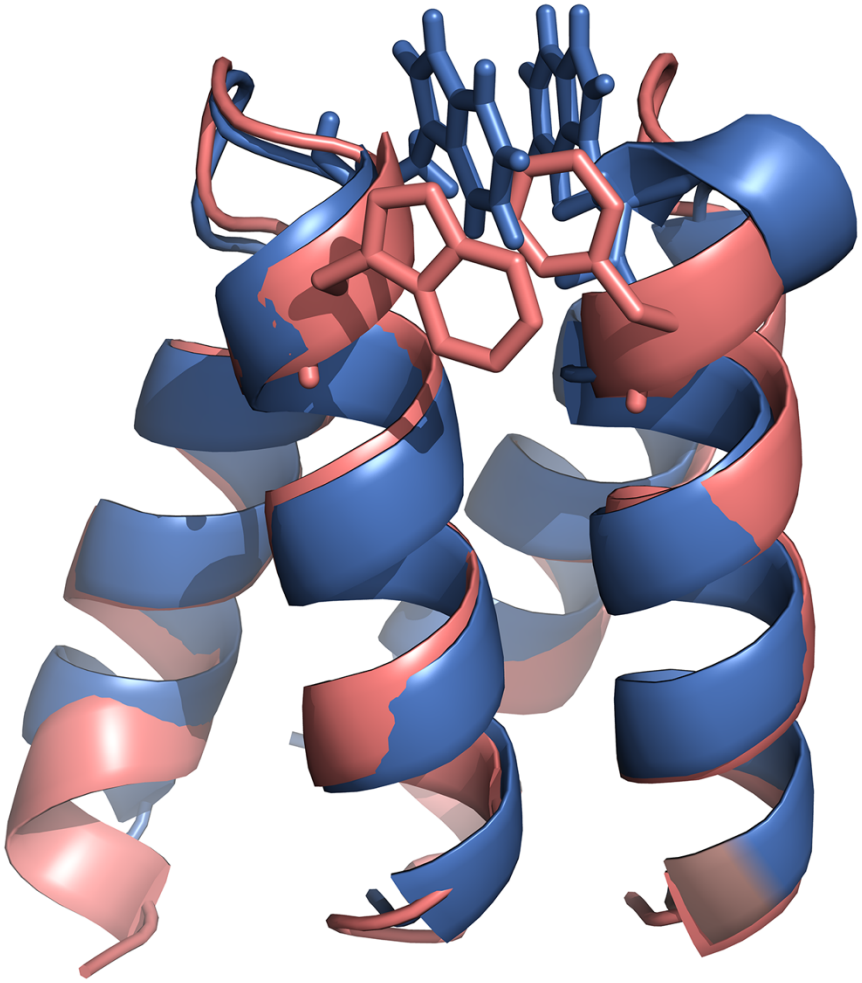

Fig. S16. Backbone overlay of the structure of the dimeric asymmetric unit of the **HEAT_R1** filament (blue) with the dimeric tandem repeat (pink) corresponding to residues 79-139 of αRep-n4-a (PDB ID: 3LTJ). The inner (concave) surfaces of the respective assemblies are oriented proximal to the viewer. Note that the formation of the Trp-Trp interaction between peptide molecules in the asymmetric unit of **HEAT_R1** causes the second molecule to deviate from the expected conformation at the turn surface to accommodate the interaction. The alignment was generated using the Super command in PyMOL.

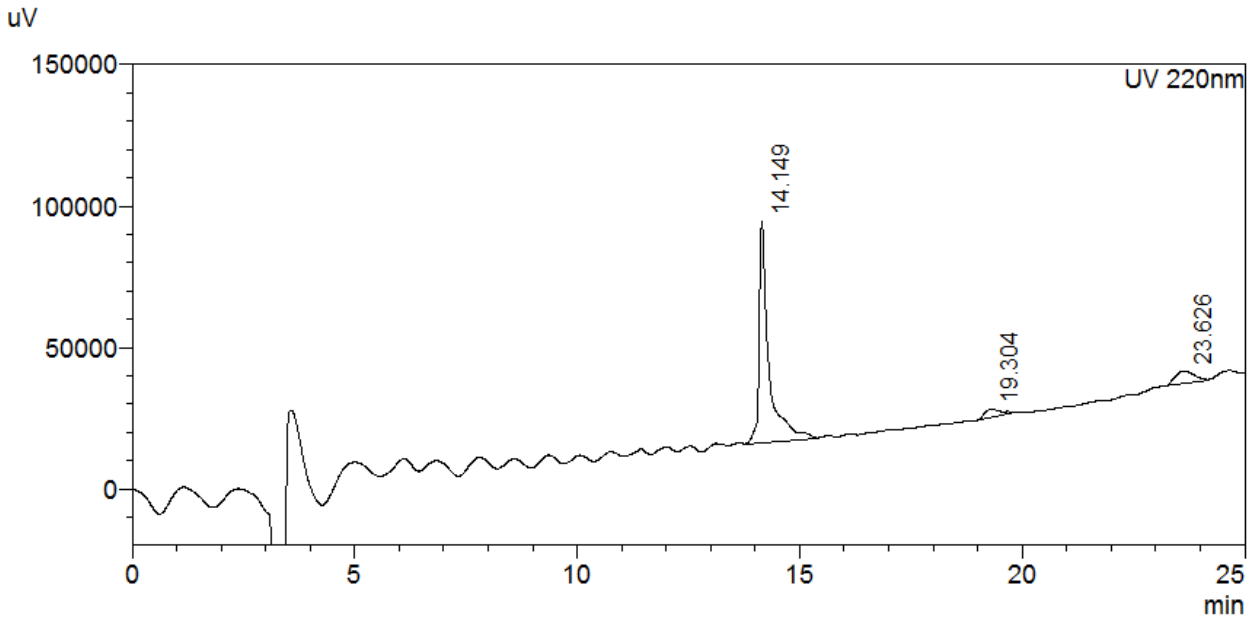

Fig. S17. Reverse-phase analytical HPLC trace of **HEAT_R1_W17F**.

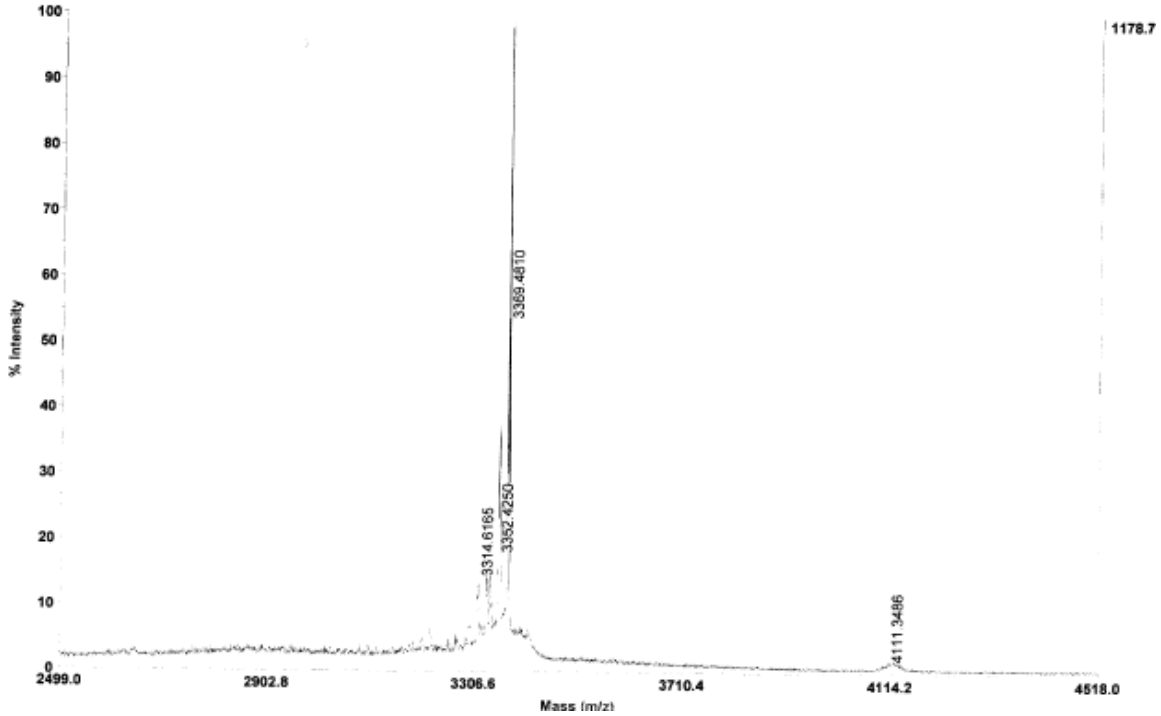

Fig. S18. MALDI-TOF mass spectrum of **HEAT_R1_W17F**.

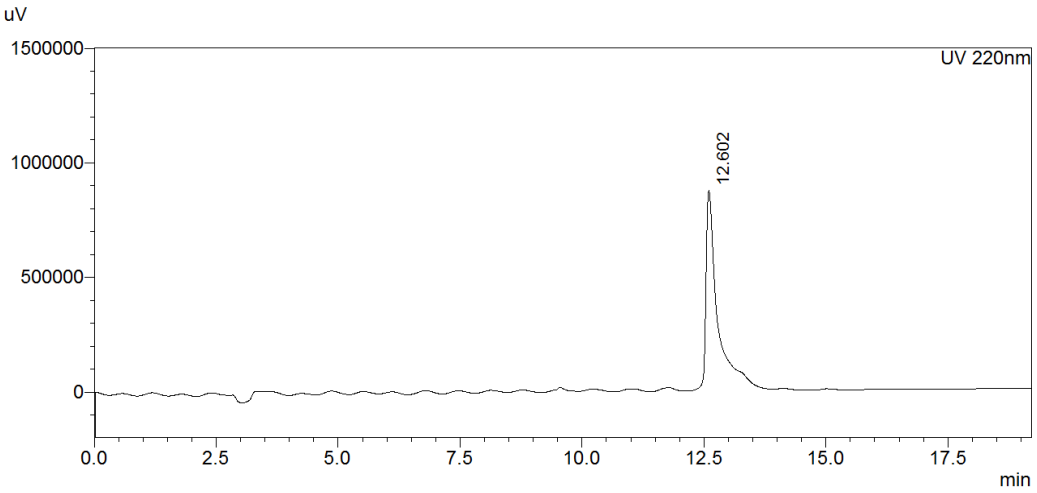

Fig. S19. Reverse-phase analytical HPLC trace of **HEAT_R1_AW.**

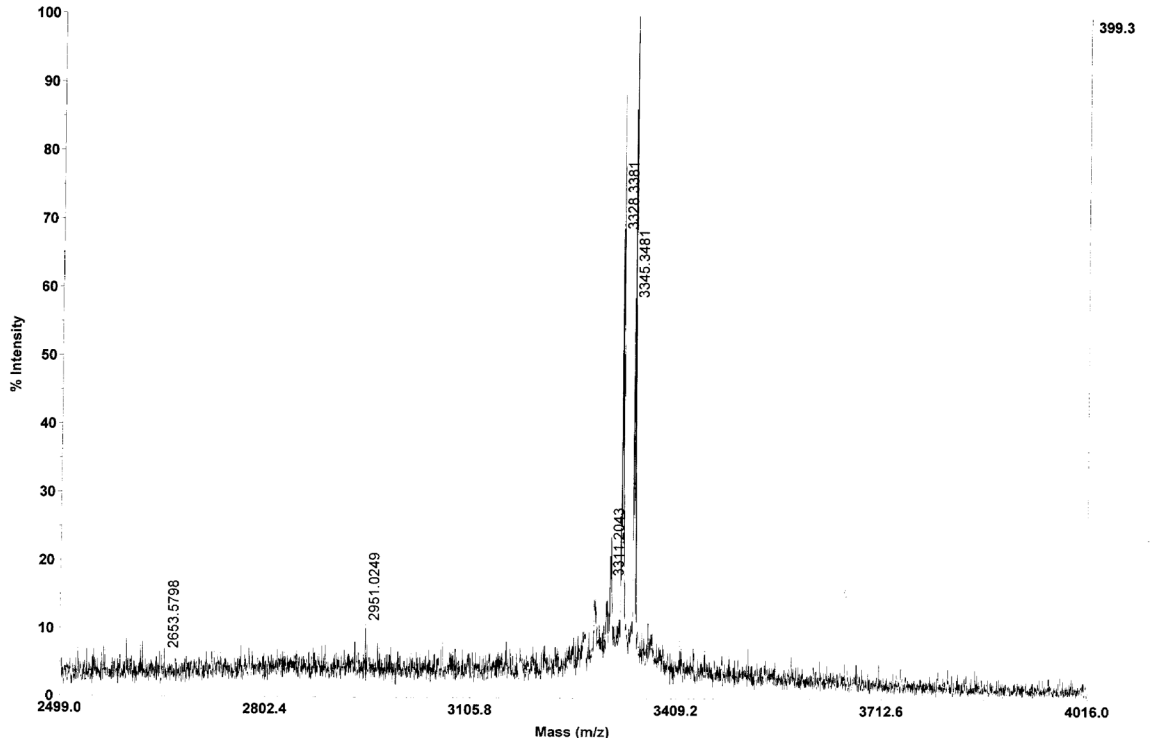

Fig. S20. MALDI-TOF mass spectrum of **HEAT_R1_AW.** The main peak at m/z of 3345 Dalton corresponds to the parent ion, while the peaks at lower mass correspond to successive loss of water molecules.

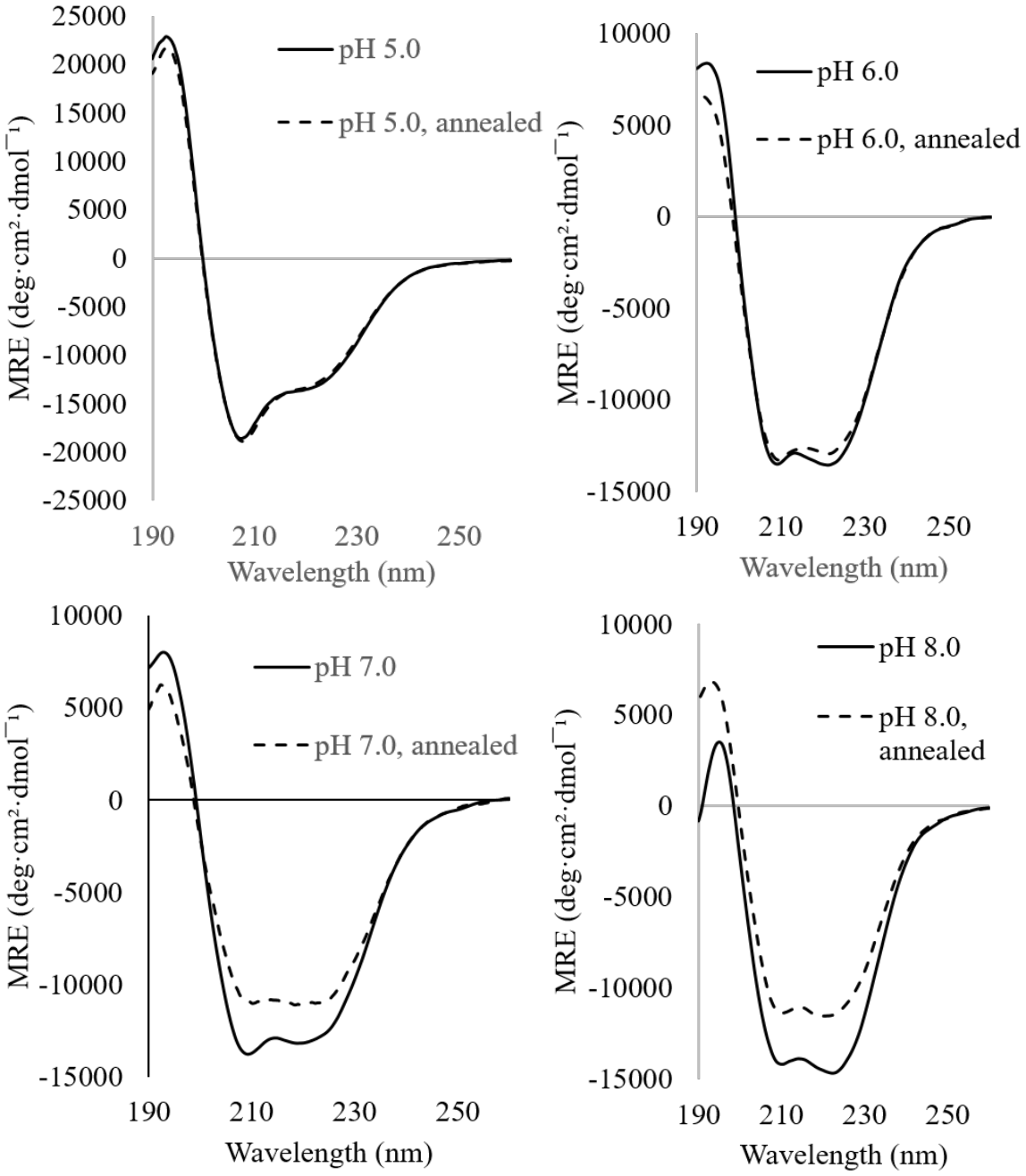

Fig. S21. CD spectra for **HEAT_R1_AW** at pH 5.0, pH 7.0, and pH 8.0 (all taken at 250μM peptide concentrations). Buffers were 10 mM Acetate (pH 5.0), 10 mM MOPS (pH 7.0), and 10 mM TAPS (pH 8.0).

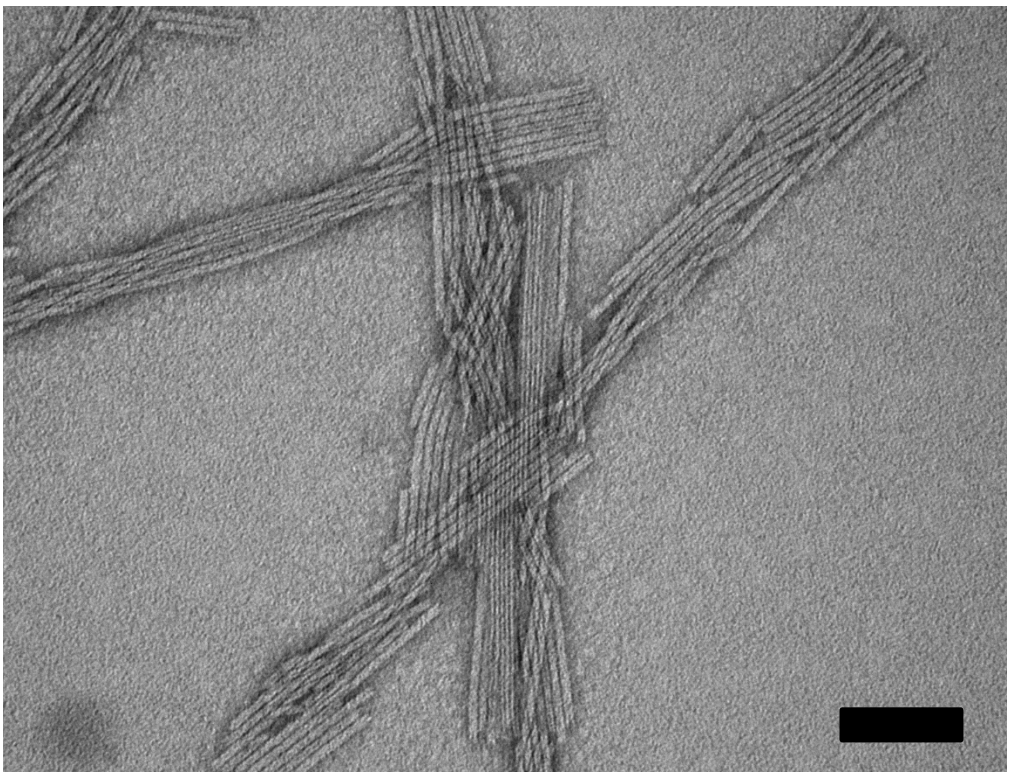

Fig. S22. Representative negative-stain TEM of **HEAT_R1_AW**. Strong lateral association was seen at every tested condition. Scale bar is 100 nm.

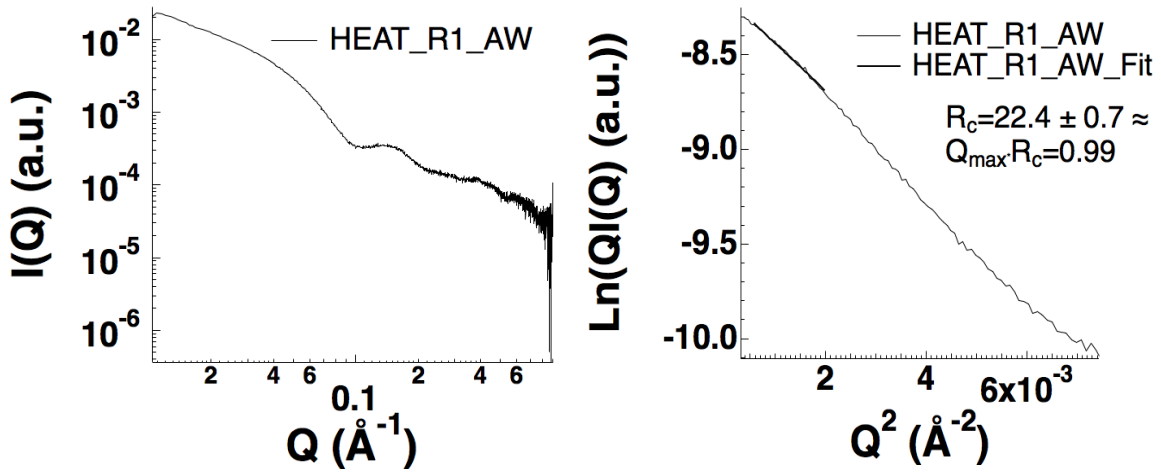

Fig. S23. SAXS scatter (left) and Guinier (right) curves for **HEAT_R1_AW**. R_c is reported in Å.

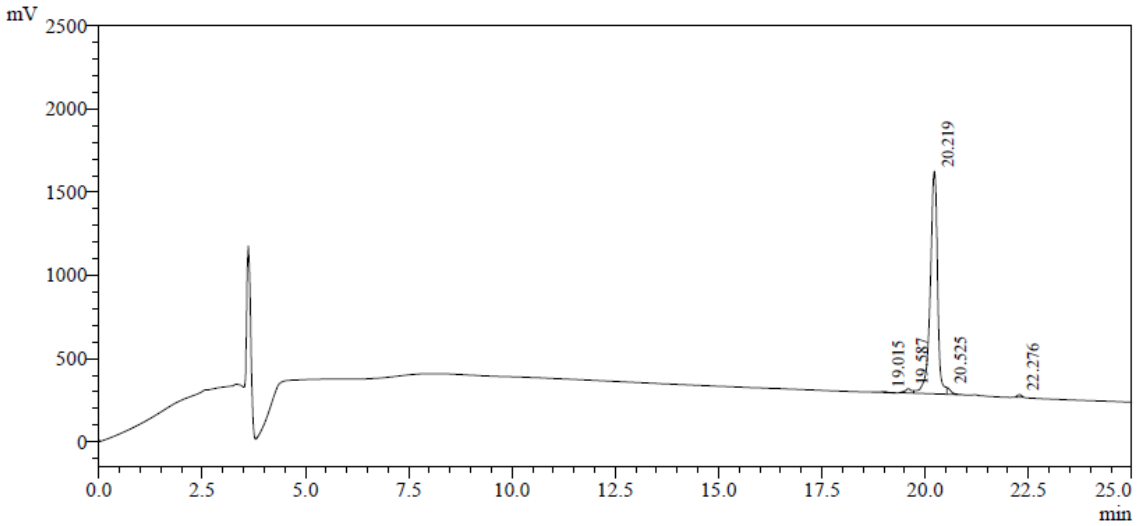

Fig. S24. Reverse-phase analytical HPLC trace of **HEAT_dimer.**

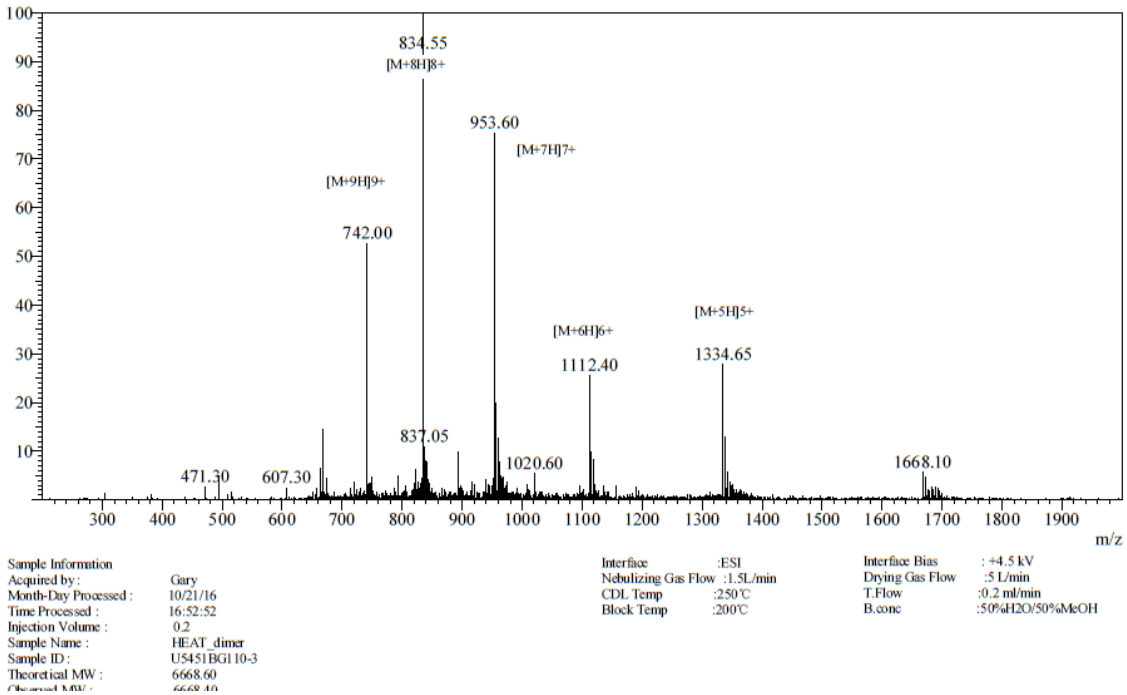

Fig. S25. ESI mass spectrum of **HEAT_dimer**.

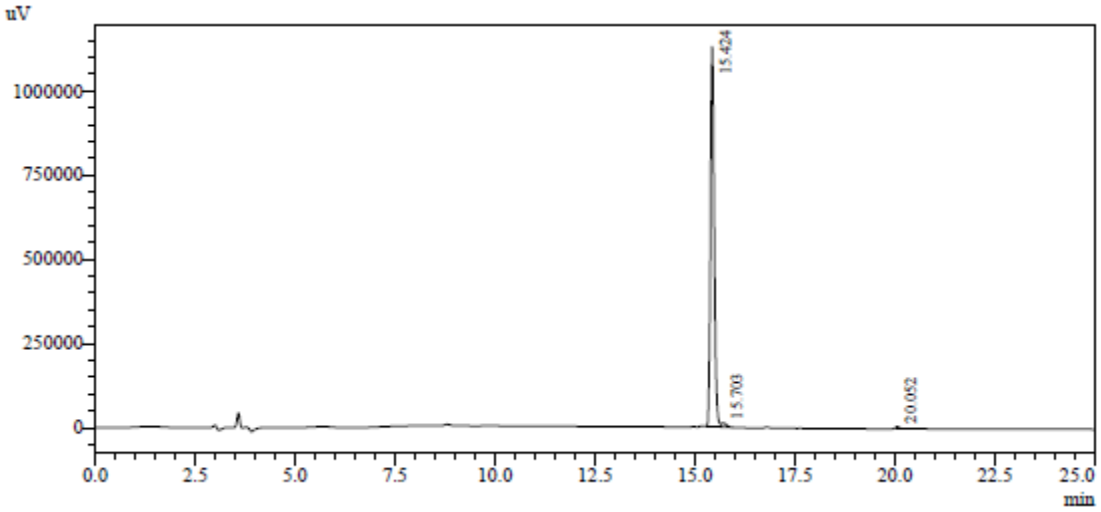

Fig. S26. Reverse-phase analytical HPLC trace of **LRV_dimer.**

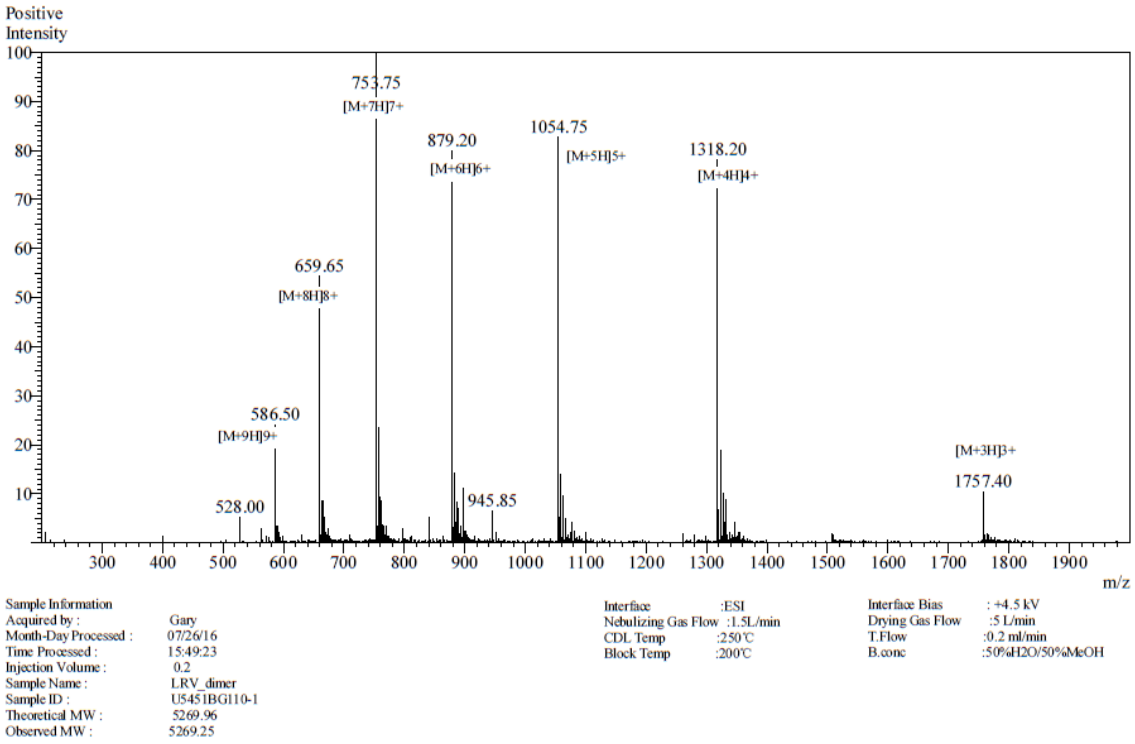

Fig. S27. ESI mass spectrum of **LRV_dimer.**

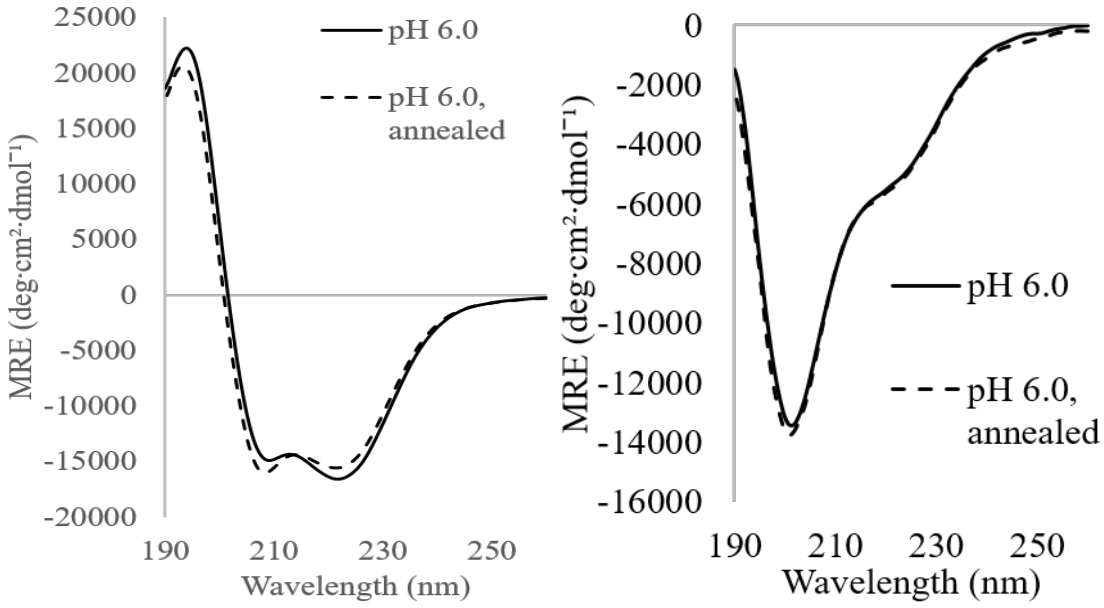

Fig. S28. CD spectra of **LRV_dimer** (left) and **HEAT_dimer** (right) at pH 6.0 (250 μM peptide concentration, 10 mM MES).

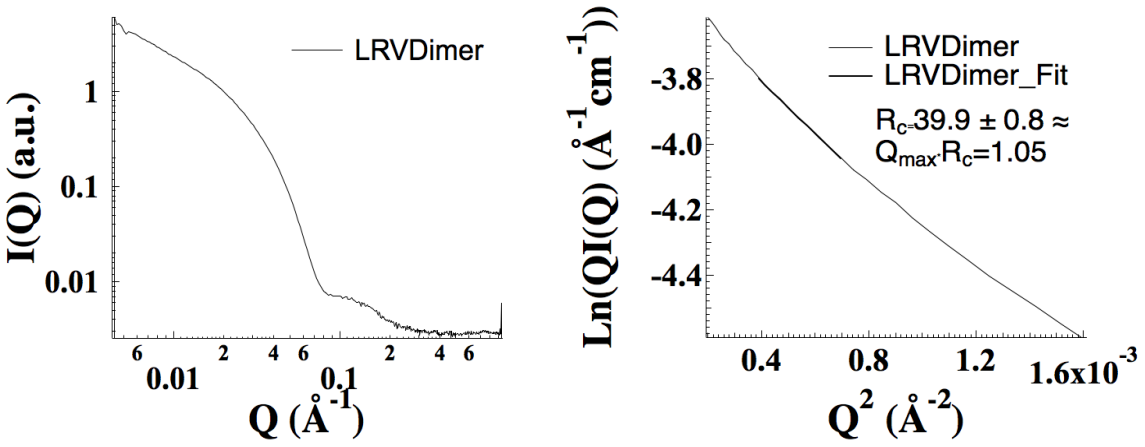

Fig. S29. SAXS scatter (left) and Guinier (right) curves for **LRV_Dimer**. R_c is reported in Å.

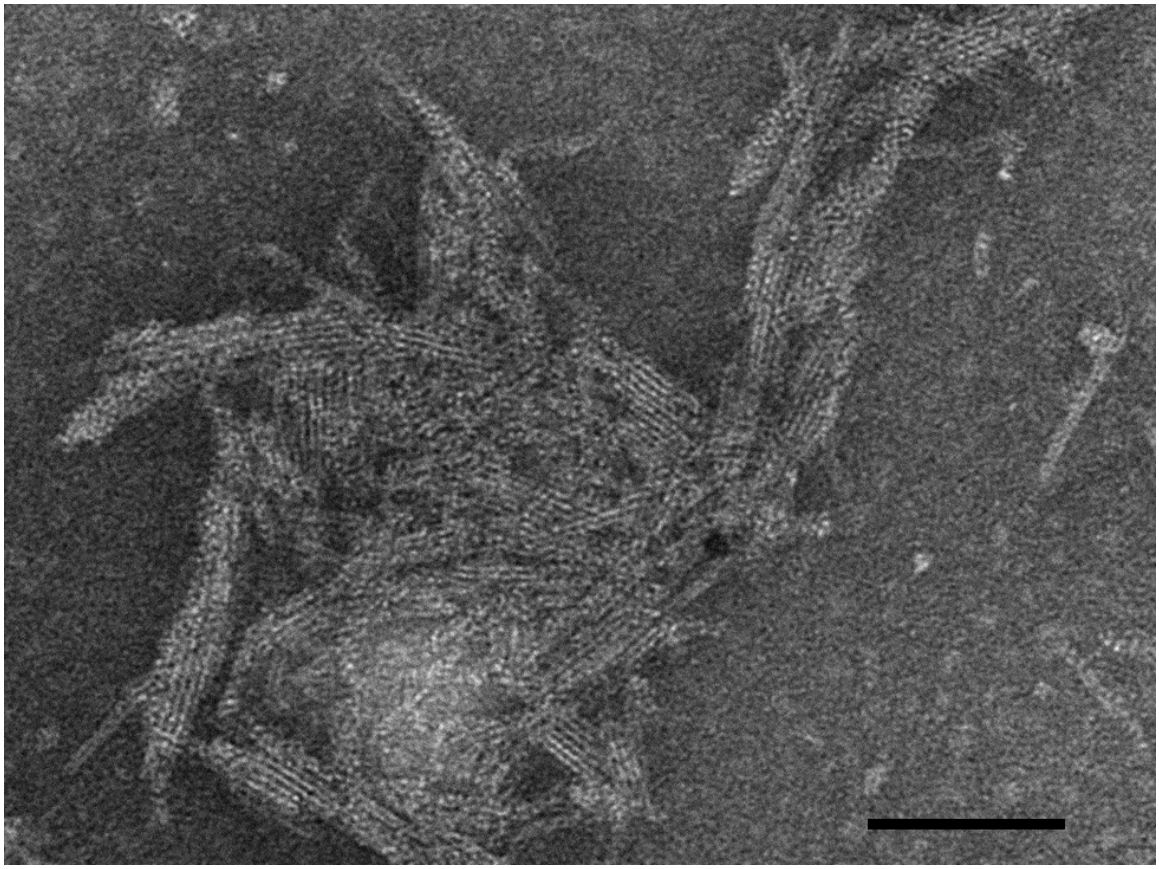

Fig. S30. Representative TEM of assemblies of **HEAT_dimer**. Short nanotubes with a high propensity for lateral aggregation were observed. Scale bar is 100 nm.

References

1. Li X, Mooney P, Zheng S, Booth C R, Braunfeld M B, Gubbens S, Agard D A, Cheng Y. (2013) Electron counting and beam-induced motion correction enable near-atomic-resolution single-particle cryo-EM. *Nat Methods 10*: 584-590.
2. Mindell J A, Grigorieff N. (2003) Accurate determination of local defocus and specimen tilt in electron microscopy. *J Struct Biol 142*: 334-347.
3. Tang G, Peng L, Baldwin P R, Mann D S, Jiang W, Rees I, Ludtke S J. (2007) EMAN2: an extensible image processing suite for electron microscopy. *J Struct Biol 157*: 38-46.
4. Egelman E H. (2000) A robust algorithm for the reconstruction of helical filaments using single-particle methods. *Ultramicroscopy 85*: 225-234.
5. Frank J, Radermacher M, Penczek P, Zhu J, Li Y, Ladjadj M, Leith A. (1996) SPIDER and WEB: processing and visualization of images in 3D electron microscopy and related fields. *J Struct Biol 116*: 190-199.
6. Kelley L A, Mezulis S, Yates C M, Wass M N, Sternberg M J E. (2015) The Phyre2 web portal for protein modeling, prediction and analysis. *Nat Protoc 10*: 845-858.
7. Guellouz A, Valerio-Lepiniec M, Urvoas A, Chevrel A, Graille M, Fourati-Kammoun Z, Desmadril M, van Tilbeurgh H, Minard P. (2013) Selection of specific protein binders for pre-defined targets from an optimized library of artificial helicoidal repeat proteins (alphaRep). *PLoS One* 8: e71512.
8. Pettersen E F, Goddard T D, Huang C C, Couch G S, Greenblatt D M, Meng E C, Ferrin T E. (2004) UCSF chimera - A visualization system for exploratory research and analysis. *J Comput Chem 25*: 1605-1612.
9. Adams P D, Afonine P V, Bunkoczi G, Chen V B, Davis I W, Echols N, Headd J J, Hung L W, Kapral G J, Grosse-Kunstleve R W, McCoy A J, Moriarty N W, Oeffner R, Read R J, Richardso D C, Richardson J S, Terwilliger T C, Zwart P H. (2010) PHENIX: a comprehensive Python-based system for macromolecular structure solution. *Acta Crystallogr D Biol Crystallogr 66*: 213-21.
10. Williams C J, Headd J J, Moriarty N W, Prisant M G, Videau L L, Deis L N, Verma V, Keedy D A, Hintze B J, Chen V B, Jain S, Lewis S M, Arendall W B 3rd, Snoeyink J, Adams P D, Lovell S C, Richardson J S, Richardson D C. (2018) MolProbity: More and better reference data for improved all-atom structure validation. *Protein Sci 27*: 293-315.
11. Song Y, DiMaio F, Wang R Y, Kim D, Miles C, Brunette T, Thompson J, Baker D. (2013) High-resolution comparative modeling with RosettaCM. *Structure 21*: 1735-1742.
12. Afonine PV, Klaholz BP, Moriarty NW, Poon BK, Sobolev OV, Terwilliger TC, Adams PD, Urzhumtsev A. (2018) New tools for the analysis and validation of cryo-EM maps and atomic models. *Acta Crystallogr D Struct Biol* 74: 814-840.